
Degassing as the Main Ore-Forming Process at the Giant Imiter Ag–Hg Vein Deposit in the Anti-Atlas Mountains, Morocco

Gilles Levresse, Mohammed Bouabdellah,
Alain Cheilletz, Dominique Gasquet, Lhou Maacha,
Jordi Tritlla, David Banks and Azizi Samir Moulay Rachid

Abstract

The giant Imiter epithermal Ag–Hg vein deposit in the Anti-Atlas Mountains of southern Morocco formed during a major episode of mineralization linked with Ediacaran volcanism at ca. 550 Ma. Silver was

G. Levresse (✉) · J. Tritlla
Programa de Geofluidos, Centro de Geociencias
UNAM-Campus Juriquilla, AP 1-253, CP 76230
Juriquilla, Querétaro, Mexico
e-mail: glevresse@geociencias.unam.mx

M. Bouabdellah
Laboratoire des Gîtes Minéraux, Hydrogéologie &
Environnement, Faculté Des Sciences, Université
Mohammed Premier, 60000 Oujda, Morocco

A. Cheilletz
ENSG, Géoresources, Université de Lorraine, 2 rue
du Doyen Marcel Roubault, 54518
Vandoeuvre-les-Nancy, France

D. Gasquet
Université de Savoie Mont Blanc, SceM-EDYTEM,
CNRS-UMR 5204, Campus Scientifique,
73376 Le Bourget du Lac Cedex, France

L. Maacha
Managem Group, Twin Center, Tour A, Angle
Boulevards Zerkouni et al Massira al Khadra, B.
P. 5199, 20000 Casablanca, Morocco

J. Tritlla
Repsol Exploración, Paseo de la Castellana 280,
28046 Madrid, Spain

D. Banks
School of Earth Sciences, University of Leeds, Leeds
LS2 9JT, UK

A.S. Moulay Rachid
AXMINE Company, Yougoslavie Avenue,
Immeuble106/6, Guéliz, 40000 Marrakech, Morocco

deposited during two main epithermal mineralizing events referred to as epithermal-quartz (ESE-Qz) and epithermal-dolomite (ESE-Dol) stages under distinct stress fields (i.e., WNW-ESE and N-S shortening directions), and is confined to the late Neoproterozoic, N60–90° E-trending, transcrustal Imiter fault zone. Economic orebodies are aligned mainly along the interface between sedimentary and volcanic units of lower and upper Cryogenian age. The ore mineralogy consists principally of Ag–Hg amalgam, argentite, polybasite, pearceite, tetrahedrite-tennantite, proustite-pyrargyrite, imiterite, acanthite, arsenopyrite, pyrite, sphalerite, and galena. Gangue constituents are dominated by quartz (ESE-Qz stage) and dolomite (ESE-Dol stage). Wall-rock alteration is well developed and includes silicification and dolomitization, and minor propylitization and kaolinitization. Fluid inclusion data indicate that the mineralizing fluids evolved through time, from a mean temperature of ~ 180 °C and salinity of ~ 10 wt% NaCl during ESE-Qz stage I, to a mean temperature of ~ 165 °C and salinity of ~ 24 wt% NaCl equiv during ESE-Dol stage II. Calculated trapping pressures, in the range of 1.1–0.9 kbar, exclude fluid unmixing “effervescence” as a viable ore depositional mechanism. Conversely, halogen compositions suggest the involvement of magmatic brines and evolved seawater. Stable (C, O, S) and radiogenic (Pb, Re/Os) isotope data, together with noble gas isotope compositions, are consistent with various degrees of mixing between mantle and crustal sources along the fluid flow path. Collectively, these data suggest that degassing of CO₂ and SO₂ during epithermal mineralization and related fluid/rock interactions led to local redox-potential decreases and pH increases that resulted in preferential deposition of massive amounts of native Hg-rich silver instead of Ag and Hg sulphide minerals.

1 Introduction

The first mining activity documented in the world-class Imiter Ag–Hg district dates to the Almohad Dynasty in the 12th Century (Leistel and Qadrouci 1991). In more recent times, the deposit was rediscovered during a campaign of aerial prospecting carried out in 1951 by the Office National des Hydrocarbures et des Mines (ONHYM; formerly BRPM). In 1969, Omnium Nord Africain Group (ONA) and ONHYM created the so-called “Société Métallurgique d’Imiter” (SMI) to re-process tailings by cyanidation (650,000 t at 300 ppm Ag). In parallel, continuing exploration delineated significant new

proven reserves of silver. Underground mining began in 1978 and continues to the present. Production has increased exponentially from 40 to 250 Mt of Ag/yr since the creation of SMI in 1969. Continued intensive exploration over the past 10 years has outlined three additional orebodies referred to as Igoudrane, Puits IV, and Imiter South. As a result, silver reserves have grown to more than 10,000 t with mine life being extended an additional 15 years (Newman 2009). Average silver grades range from 300 to 1,000 g/t and locally can reach 5,000 g/t. Current annual production is about 200–300 t Ag; remaining mineral resources are estimated at 3,000 Mt Ag (Newman 2009).

Based on these production estimates, the Imiter deposit is considered one of the largest silver deposits in the world (Katrivanos 2015). To explain the origin of such a huge silver concentration, diverse genetic models have been proposed (Leistel and Qadrouci 1991; Baroudi et al. 1999; Levresse et al. 2004). These models range from syngenetic (Vargas 1983; Popov et al. 1986; Guillou et al. 1988; Popov 1995) to epigenetic (Leistel and Qadrouci 1991). From 2000 onward, most workers have advocated epithermal mineralizing processes (Levresse 2001; Cheilletz et al. 2002; Levresse et al. 2004). However, despite an impressive number of geochemical investigations, the genesis of the Imiter Ag deposit remains uncertain, particularly the origin(s) of the ore-forming fluids, sources of heat and metal components, mechanism(s) of ore deposition, and the age of mineralization. The objective of the present contribution is to update the geologic history, mineralization, and paragenesis of the Imiter deposit, and more importantly to contribute, with new data on fluid inclusions, halogens, and lead isotopes, constraints on the source(s) of sulphur and metals. Based on these newly acquired data, we provide important insights into the origin and evolution of the mineralizing system, together with implications for understanding ore-forming processes in the context of local Neoproterozoic magmatism.

2 District Geology

The Ag–Hg Imiter deposit (32° 43' N Lat; 5° 36' W Long) is located in the northern part of the Precambrian Saghro massif (Fig. 1). This massif forms part of the 680–580 Ma Pan African Anti-Atlas orogenic belt, north of the West African Craton margin (Ennih and Liégeois 2001). Regional and local geology of the district have been extensively investigated over the past several decades, resulting in a wealth of scientific information including geological maps at different scales, university theses, research papers, and unpublished mining company reports (Leistel and Qadrouci 1991; Pašava 1994; Ouguir et al. 1996; Baroudi et al. 1999; Levresse 2001; Fekkak et al.

2001; Cheilletz et al. 2002; Levresse et al. 2004; Gasquet et al. 2005; Tuduri et al. 2005). Accordingly, only a summary relevant to the present synthesis is given below.

The oldest rocks assigned to the Saghro Group (Thomas et al. 2004) were deposited on the Neoproterozoic basement. Strata of the Saghro Group form a lower complex consisting of a strongly folded Cryogenian succession of greenschist-facies greywacke and organic-rich black shale, locally intruded by ca. 570–580 Ma granodioritic to dioritic intrusions (e.g., Taouzakt and Igoudrane plutons). The black shales, which host the majority of Imiter silver mineralization, were deposited at the outer part of a passive continental margin that developed in an extensional back-arc environment (Marini and Ouguir 1990; Ouguir et al. 1996).

Unconformably overlying the clastic sedimentary rocks of the lower complex are Ediacaran volcanic and volcanoclastic rocks of the upper complex assigned to the Ouarzazate Supergroup (580–560 Ma; Mifdal and Peucat 1985). The main lithologies are immature conglomerate at the base grading upward into andesitic lava flows and felsic ignimbrites (572–550 ± 3 Ma; U/Pb zircon) and associated cogenetic granites (580–570 Ma, U/Pb zircon) (Cheilletz et al. 2002). At the end of the Neoproterozoic, a marine transgression invaded all of the Anti-Atlas and deposited the so-called “Adoudounian” (Lower Cambrian) succession. This succession is composed of interbedded carbonate, purple shale with minor siltstone, evaporites, greywacke (Piqué et al. 1999; Álvaro et al. 2014) and mafic sills dated at 529 ± 3 Ma (Ducrot and Lancelot 1977, recalculated) and 531 ± 5 Ma (Gasquet et al. 2005).

Silver mineralization occurs within the Cryogenian black shale and partly in the Ediacaran volcanic rocks. More importantly, this mineralization is localized along the Late Neoproterozoic, N60–90° E-trending transcrustal Imiter fault zone (Fig. 1), which straddles the boundary between the lower and upper complexes. The prominent Imiter fault zone consists of complex arrays of N90° E and N60–70° E faults that exhibit, at map scale, apparent sinistral pull-apart

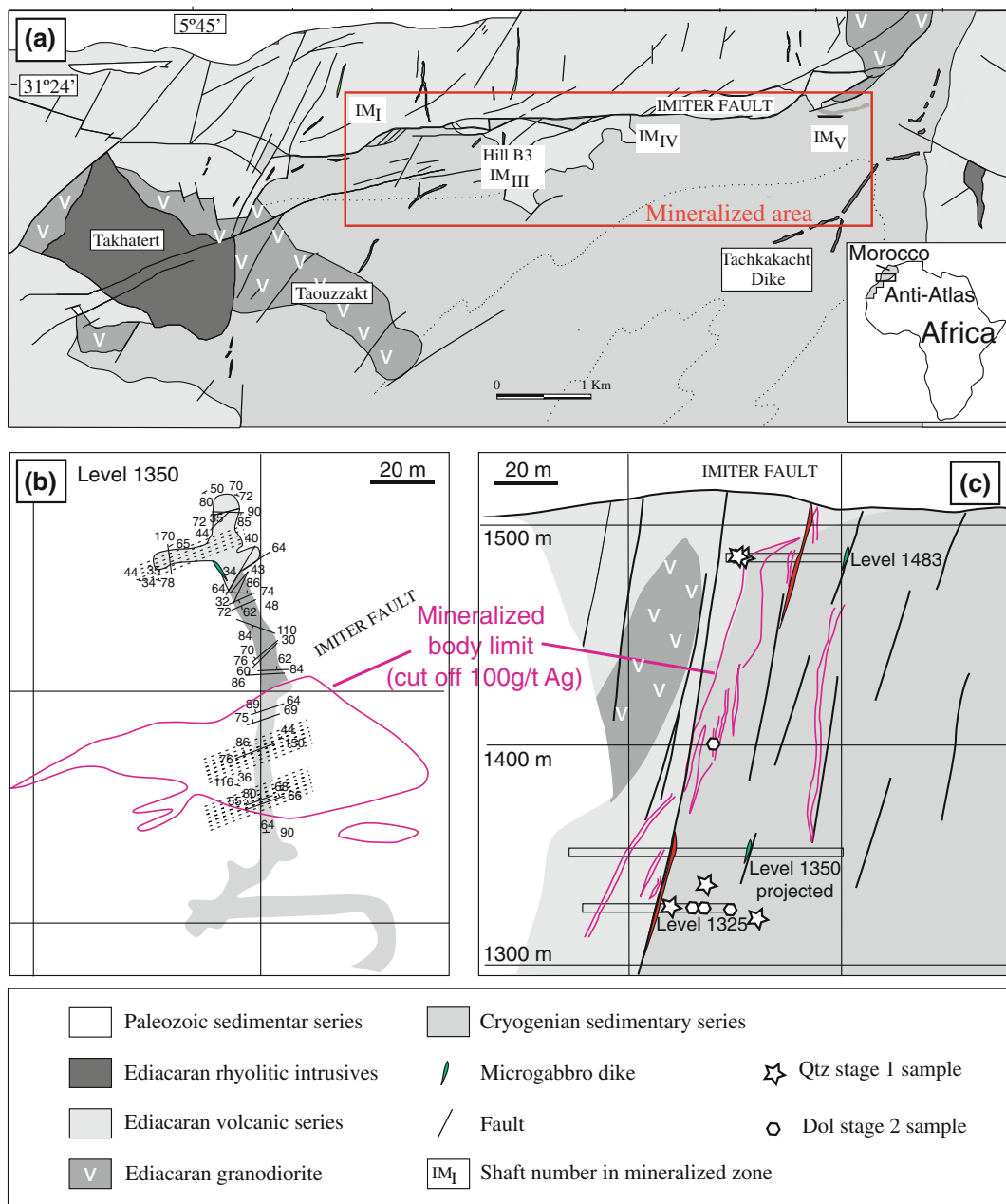


Fig. 1 **a** Geological map of Imiter Ag-Hg deposit area, Anti-Atlas, Morocco. Modified from Leistel and Qadrouci (1991). **b** Horizontal projection of silver ore body in B3 Hill workings (1350 m is altitude of this mining level);

c N-S synthesized geological cross section drawn for B3 Hill (white stars indicate sampling locations within the mine)

structures (Ouguir et al., 1994; 1996; Tuduri et al. 2005). Reactivation of the Imiter fault system during the Hercynian orogeny facilitated the injection of variously aged dike swarms of

diverse composition ranging from trachyandesite to high-K microsyenite and microgabbro. One microsyenite dike has been dated at ca. 200–204 Ma ($^{40}\text{Ar}/^{39}\text{Ar}$ on biotite and K-feldspar;

Borisenko et al. 2013). The Takhatert rhyolite is characterized by a well-defined, domal structure (Fig. 1), suggesting that it is a hypabyssal body. The felsic dikes, including the Tachkakacht dike, are similar in composition and age to the Takhatert rhyolite (547 ± 8 Ma; U/Pb zircon; Levresse 2001). Pan-African regional metamorphism under greenschist-facies conditions resulted in the formation of chlorite-, muscovite-, and pyrophyllite-bearing mineral assemblages, with peak conditions reaching 350 °C and up to 3 kb (Thomas et al. 2004). Higher temperatures were attained locally in the aureoles of post-kinematic intrusions (547 ± 26 Ma; Thomas et al. 2004).

3 Mineralization

Silver mineralization is structurally controlled within a system of ENE-WSW- to E-W-trending, variously dipping, transpressive to transtensional structures. These structures include vein swarms, veinlets, cemented breccias within veins, and lensoidal or pocket-like masses and fillings of echelon tension gashes. Most, if not all, of the exploited silver orebodies are confined to the prominent Imiter fault zone (Fig. 1), which is typically aligned along the interface between the lower and upper lithostratigraphic complexes. In addition to the Ag–Hg ores within the mineralized structures, Ag–Hg minerals also occur disseminated in the basal conglomerate and black shales. Overall, the veins are up to 4 m wide and extend laterally from a few meters to more than 1 km, are spaced 50–100 m apart, strike N160° E, and dip steeply (70° to ~90°).

Where Ediacaran volcanic rocks of the upper complex are present (e.g., Hill B3; Fig. 1), the orebodies are largest within the basal conglomerate and are continuous through the fractured rock within the Imiter fault zone. Silver mineralization has never been found within the andesitic host rocks or the ca. 580–570 Ma granodiorite exposed at Hill B3. Both rock types seem to represent a “cap rock” for mineralization. The spatial distribution of the orebodies appears, therefore, to be linked directly to the rheology of the surrounding host rocks. In this regard, we

suggest that the foliated nature of the host rocks facilitated later fracturing, fluid flow, and emplacement of the mineralized veins.

Two principal vein systems, referred to as “Imiter 1” and “Imiter 2” have been mined both from open pits and underground workings. The Imiter I vein system consists of three variably dipping structures (F_0 , F_0 north, and F_0 south) that strike N90–N65° E. In contrast, Imiter 2 comprises three vein orebodies referred to as R_6 , R_7 , and B_3 that exhibit roughly the same geometric characteristics in terms of orientation and dip. Recent exploration in the district has delineated three new orebodies referred to as Igoudrane, Puits IV, and Imiter South (Fig. 1).

Textural relationships together with mineral assemblages indicate a complex history involving contemporaneity of replacement and open-space filling. The veins display comb, cockade, laminated, breccia, and crack-and-seal textures, suggesting that multiple mechanisms were important for trans-tensional vein formation. Early precipitated minerals are cut or brecciated, and subsequently cemented, by later phases. Collectively, these textural features indicate that mineralization took place in open spaces, and imply that the Imiter orebodies formed in a relatively shallow environment.

Spatial and temporal relationships between the silver mineralization and country rocks indicate four distinct and successive mineralizing events. From oldest to youngest, these events are: (1) recrystallization during Pan-African metamorphism of syngenetic-diagenetic pyrite hosted in Cryogenian black shale; (2) development of a discrete, base-metal mineral assemblage (BMS) adjacent to metamorphic aureoles induced by intrusion of the granodiorite (ca. 572 Ma); (3) formation of epithermal silver mineralization (i.e., ESE stage) dated at ca. 550 Ma (Cheilletz et al. 2002; Levresse et al. 2004), which constitutes the bulk of exploited mineralization in Imiter; and (4) Ag–Hg remobilization at 255 Ma (Borisenko et al. 2013). Cross-cutting relationships and mineral assemblages indicate that the epithermal silver mineralization occurred during two main stages referred to as epithermal-quartz (ESE-Qz) and

epithermal-dolomite (ESE-Dol) (Levresse 2001; Cheilletz et al. 2002; Levresse et al. 2004; Burniaux and Williams-Jones 2006; Tuduri et al. 2005; Borisenko et al. 2013; this study). Each stage is characterized by particular styles, ore and gangue mineral assemblages, and silver grades (Fig. 2).

The first silver mineralizing stage (ESE-Qz Stage I) formed during a dextral transpressive event under WNW-ESE shortening (Tuduri et al. 2005). Principal minerals are quartz (Qz-1), Ag–Hg amalgam, argentite, polybasite, pearceite, tetrahedrite-tennantite, proustite-pyrargyrite, imiterite, acanthite,

arsenopyrite, pyrite, and galena. The following stage (ESE-Dol Stage II) resulted from reopening of the earlier veins in response to normal, sinistral regime (Tuduri et al. 2005). This stage comprises pink dolomitic alteration and an associated mineral assemblage dominated by Ag–Hg amalgam, acanthite, tetrahedrite-tennantite, galena, sphalerite, pyrite, chalcopryrite, and arsenopyrite. The type of gangue mineral (i.e., quartz vs. dolomite) appears to be strongly controlled by lithology of the host rocks (Ediacaran volcanics vs. Cryogenian black shale).

Within the Imiter deposit, the most highest grade impressive orebodies are developed along

Mineralogical stage		$\delta^{13}\text{C}$	$\delta^{18}\text{O}$	$\delta^{34}\text{S}$	$\frac{^{206}\text{Pb}/^{204}\text{Pb}}{^{207}\text{Pb}/^{204}\text{Pb}}$	$\frac{^{187}\text{Os}}{^{188}\text{Os}}$	^4He
Qtz stage 1							
quartz-1							1,05-1,84Ra
muscovite							
pyrite				-11,9 to -4,5			
arsenopyrite							
chalcopryrite				-2,4			
sphalerite				-10,9 to -8,0		0,199	
galena				-10,0 to -4,8		0,185	0,76Ra
tetrahedrite							
Ag-amalgam						0,183 to 0,195	
argentite							
polybasite							
pyargyrite						0,143	
proustite							
Dol stage 2							
dolomite		-10.5 to -8.1	-13.4 to -0.1				0,89Ra
pyrite				-8,0 to -4,1			
arsenopyrite				-22,6 to -1,8			
chalcopryrite				-3,2			
sphalerite				-9,3 to -5,0			
galena				-19,6 to -7,1	15,55 to 15,59 18,11 to 18,17		
Ag-amalgam							
argentite							
polybasite							
imiterite							
pyargyrite				-7,0		0,147	1,21Ra
proustite							
pearcite							
cinnabar				-27,7			

Fig. 2 Paragenetic succession for Imiter Ag–Hg deposit and ranges of isotopic values for C, O, S, Pb, Os, and He during epithermal silver mineralization (Pašava 1994; Levresse 2001; Levresse et al. 2004; this study)

extensive fault zones and related breccias that in places contain tens of kilograms of native silver (i.e., Ag–Hg and Ag). It is noteworthy that Hg contents of the Ag–Hg amalgam increase from quartz-dominant stage I to dolomite-dominant stage II, with Hg abundances ranging from 10 to 30 % and 20 to 40 %, respectively. Where observed, silver sulphosalts precipitated either with, or as replacements of, preexisting sulphides. Imiterite (Ag_2HgS_2) is the most common Hg-bearing sulphide and forms needles filling dolomitic geodes that are spatially associated with cinnabar and argentite (Guillou et al. 1985). Supergene oxidation is scarce and limited to upper levels of the deposit (Levresse et al. 2004). The oxidized mineral assemblage there includes milky quartz, rhodochrosite, kaolinite, erythrite, malachite, azurite, marcasite, lavendulan [$\text{NaCaCu}_5(\text{AsO}_4)_4\text{Cl}\cdot 5\text{H}_2\text{O}$], cerussite, and the iron oxides hematite and goethite.

Wall-rock alteration is weakly developed. Major types include propylitization, silicification, dolomitization, and kaolinitization. Silicification and dolomitization are prominent around the mineralized structures, whereas kaolinitization is spatially limited and paragenetically late.

4 Age of Mineralization

Based on field relationships and $^{40}\text{Ar}/^{39}\text{Ar}$ ages of hydrothermal muscovite, Levresse (2001) and Cheilletz et al. (2002) concluded that the bulk of Imiter silver mineralization occurred between 563 ± 8 and 542 ± 0.2 Ma. More recently, Borisenko et al. (2013) reported a single-crystal $^{40}\text{Ar}/^{39}\text{Ar}$ age of 255 ± 3 Ma for adularia intergrown with Qz-1 from the ESE-Qz stage and proposed a Triassic age of mineralization, coincident with early opening of the Central Atlantic Province. This new age determination suggests that the Triassic rifting event could have remobilized the primary Cryogenian Ag–Hg mineralization at Imiter, as documented in other hydrothermal deposits of the Anti-Atlas system such as the Iourim Au deposit (Gasquet et al. 2004), the Tamlalt-Menhouhou orogenic gold deposit (Pelleter et al. 2008, 2010), and the

Bou-Azzer Co–Ni–As–Au deposit (Oberthur et al. 2007).

5 Analytical Methods

5.1 Fluid Inclusion Study

A Linkam stage was used to record ice-melting temperature (T_{mi}) and homogenization temperature (T_{h}) of fluids in the ESE quartz- and dolomite-hosted inclusions. Calibrations were performed with appropriate chemicals from Merck. Measurement accuracy was about ± 0.2 °C for freezing runs and ± 1 °C for heating runs. Representative inclusions were further analyzed with a Labram-type (DilorR) Raman microprobe with a NotchR filter at the laboratory of “GeoRessources (Nancy, France); technical details are provided in Debussy et al. (2001).

Bulk crush-leach analyses were performed on quartz and dolomite separates from the ESE-Qz and ESE-Dol stages at the School of Earth Sciences, University of Leeds. The procedure has been described in detail by Banks et al. (2000). Samples were crushed to 1–2 mm size and cleaned in 18.2 MΩ water. Dry samples of 0.5–1 g were crushed to a fine powder in an agate pestle and mortar, transferred to a sample container, and the dried salts redissolved in 18.2 MΩ water. Anions (Cl^- and Br^-) were determined with a Dionex DX-500 ion chromatograph; cations (Na^+ and K^+) were determined on the same solution with an acidified LaCl_3 solution by flame emission spectroscopy. Analytical precision of these analyses was better than ± 10 % (2σ).

6 Lead Isotope Study

Lead isotope analyses were performed at Sgiker Laboratories of the Basque Country University in Bilbao, Spain, on representative galena separates from the main ore stages. About 0.10 g of powdered material and an aliquot of about 0.02 g, respectively, were digested overnight in HF– HNO_3 and evaporated to dryness. The

resulting residue was taken in HBr; Pb was isolated by conventional ion-exchange chromatography (AG1-X8 resin in HBr and HCl media). Recovered lead was evaporated to dryness, dissolved in 0.32 N HNO₃, and diluted to a final concentration of 150–200 ppb. Lead isotope ratios were measured using a ThermoNEPTUNE multicollector inductively coupled plasma-mass spectrometer (ICP-MS), and the mass fractionation was internally corrected after the addition of thallium isotope reference material NBS-997. Analytical error, determined as a total uncertainty of the results and confirmed by more than 20 analyses of lead isotope reference material NBS-981, was about 0.04 % per mass unit (2 σ), equivalent to 0.041, 0.040, and 0.039 %, respectively, for ²⁰⁶Pb/²⁰⁴Pb, ²⁰⁷Pb/²⁰⁴Pb, and ²⁰⁸Pb/²⁰⁴Pb ratios.

7 Fluid-Inclusion Microthermometry

New microthermometric measurements were performed on quartz (Qz-1) and dolomite (Dol-2) wafers from the ESE-Qz (I) and ESE-Dol (II) stages. Data are presented in Table 1 and plotted in Figs. 3 and 4. The fluid inclusions are classified as primary, pseudosecondary, or secondary according to the criteria of Roedder (1984). Based on the number of observable phases present at room temperature, four distinct fluid inclusion types (designated 1–4) are recognized: (1) liquid-vapor (L + V; Type 1); (2) liquid-vapor-one solid (L + V + S₁; Type 2); (3) liquid-vapor-two solids (L + V + S₁₋₂; Type 3); and (4) vapor (V; Type 4). All fluid inclusion types generally occur together within a trail or cluster. In Type 1 fluid inclusions, visually estimated liquid to vapor ratios are highly variable, ranging from 0.4 to 0.8. Vapor-rich inclusions (liquid/vapor <0.5) are rare, representing less than 10 % of the total.

Fluid inclusions hosted in Qz-1 are isolated and up to 50 μ m in diameter, or are grouped in clusters that show a random distribution within a single grain or growth zone. The fluid inclusions in Qz-1 are spatially associated with silver blebs

distributed along growth zones within the host quartz. Raman analyses indicate that the trapped solid phases correspond to muscovite (S₁) and sulphide (S₂). Chloride daughter minerals such as halite and sylvite have not been observed.

Fluid inclusions hosted in Dol-2 are isolated or form trails distributed along growth zones. Estimated liquid to vapor ratios are less than 0.8. Owing to the fluorescence of the dolomite, no reliable Raman data have been obtained on these fluid inclusions.

Overall, microthermometric data indicate that the mineralizing fluids evolved through time, from a mean temperature of \sim 180 °C and calculated salinity of \sim 10 wt% NaCl equiv in Qz-1, to a mean temperature of \sim 165 °C and calculated salinity of \sim 24 wt% NaCl equiv in Dol-2 (Table 1; Figs. 3 and 4).

In the T_{h(LV)} versus T_{mi} plot shown in Fig. 3, data for Qz-1 and Dol-2 display a negative correlation. Primary and pseudosecondary fluid inclusions in both minerals exhibit roughly the same T_h range of ca. 217–126 °C but fluid inclusions hosted in Dol-2 have consistently higher salinities (\sim 24 wt% NaCl equiv; Table 1). In addition, the type of host rock and fluid salinity are related. For example, data for Qz-1 samples hosted in Ediacaran volcanic rocks display a weakly isohaline-cooling path, whereas those for Qz-1 and Dol-2 samples in Cryogenian black shale exhibit a parallel negative correlation between T_{h(LV)} and T_{mi} (Fig. 3).

Raman analyses of the vapor phase related to Qz-1 reveal the occurrence of mixtures of CH₄–CO₂ or CH₄–N₂. CH₄ is commonly the predominant component (up to 52 vol.%). CO₂ and N₂ have not been found together in the same fluid inclusion. With increasing depth, N₂ proportion decreases and CH₄ proportion increases up to 100 %.

P-T reconstruction of Qz-1 fluid evolution has been determined using the intersection coordinates of calculated fluid inclusion isochores together with results of chlorite geothermometry. Accordingly, the minimum trapping pressure estimates are in the range of 1.1–0.9 kbar for the mineralizing fluid that deposited the high-grade portion of the Imiter silver orebodies.

Table 1 Microthermometric data of typical fluid inclusions of silver epithermal stages from Imiter Ag–Hg deposit

Silver epithermal mineralizing event								
Quartz-1 in volcanite			Quartz-1 in black shale			Dolomite-2 in black shale		
Inclusions	T _h (°C)	T _{mi} (°C)	Inclusions	T _h (°C)	T _{mi} (°C)	Inclusions	T _h (°C)	T _{mi} (°C)
Inc. 1	189.95	–3.70	Inc. 1	184.56	–11.24	Inc. 1	125.74	–21.32
Inc. 2	185.18	–2.56	Inc. 2	180.01	–9.59	Inc. 2	137.25	–21.21
Inc. 3	176.23	–4.10	Inc. 3	178.37	–13.05	Inc. 3	137.66	–19.87
Inc. 4	217.82	–6.62	Inc. 4	172.87	–13.40	Inc. 4	139.85	–21.09
Inc. 5	214.77	–5.06	Inc. 5	167.91	–15.45	Inc. 5	147.14	–27.43
Inc. 6	206.03	–5.53	Inc. 6	167.91	–16.27	Inc. 6	151.89	–21.20
Inc. 7	199.19	–5.69	Inc. 7	174.00	–16.18	Inc. 7	196.22	–10.61
Inc. 8	196.53	–8.67	Inc. 8	166.59	–15.21	Inc. 8	206.60	–13.66
Inc. 9	193.95	–9.15	Inc. 9	162.58	–14.86	Inc. 9	208.59	–13.66
Inc. 10	189.99	–9.03	Inc. 10	159.96	–13.54	Inc. 10	208.46	–20.20
Inc. 11	191.55	–8.79	Inc. 11	161.70	–12.88	Inc. 11	190.99	–21.20
Inc. 12	185.60	–9.22	Inc. 12	163.90	–11.91	Inc. 12	194.08	–22.41
Inc. 13	185.60	–8.99	Inc. 13	161.30	–9.91	Inc. 13	186.44	–20.79
Inc. 14	187.65	–8.90	Inc. 14	168.51	–9.87	Inc. 14	193.02	–17.52
Inc. 15	187.65	–7.62	Inc. 15	172.71	–10.92	Inc. 15	207.81	–15.90
Inc. 16	183.18	–7.95	Inc. 16	170.71	–8.02	Inc. 16	194.37	–15.03
Inc. 17	178.78	–7.95	Inc. 17	184.55	–6.93	Inc. 17	190.54	–27.23
Inc. 18	176.40	–9.25	Inc. 18	147.52	–7.69	Inc. 18	170.50	–29.09
Inc. 19	176.18	–8.94	Inc. 19	148.23	–7.25	Inc. 19	163.10	–27.09
Inc. 20	173.84	–8.01	Inc. 20	146.69	–10.62	Inc. 20	159.90	–25.90
Inc. 21	168.36	–7.21	Inc. 21	157.71	–18.32	Inc. 21	165.47	–22.66
Inc. 22	175.99	–7.33	Inc. 22	151.59	–17.58	Inc. 22	161.97	–23.10
Inc. 23	176.32	–6.51	Inc. 23	155.35	–16.48	Inc. 23	161.97	–22.29
Inc. 24	179.94	–7.29	–	–	–	Inc. 24	162.43	–22.14
Inc. 25	180.88	–6.59	–	–	–	Inc. 25	166.23	–21.33
Inc. 26	178.97	–5.46	–	–	–	Inc. 26	169.41	–22.58
Inc. 27	179.64	–6.16	–	–	–	Inc. 27	169.70	–22.33
Inc. 28	181.24	–5.85	–	–	–	Inc. 28	173.08	–22.72
Inc. 29	183.22	–5.26	–	–	–	Inc. 29	170.75	–20.90
Inc. 30	189.94	–5.73	–	–	–	Inc. 30	173.54	–20.77
Inc. 31	188.29	–5.81	–	–	–	Inc. 31	167.69	–20.77
Inc. 32	188.06	–6.64	–	–	–	Inc. 32	177.60	–20.55
Inc. 33	189.89	–6.57	–	–	–	Inc. 33	178.23	–20.33
Inc. 34	192.33	–6.45	–	–	–	Inc. 34	178.12	–19.21
Inc. 35	193.70	–6.23	–	–	–	Inc. 35	174.76	–18.94
Inc. 36	194.75	–6.78	–	–	–	Inc. 36	174.36	–19.10
Inc. 37	196.97	–6.66	–	–	–	Inc. 37	181.37	–20.73

(continued)

Table 1 (continued)

Silver epithermal mineralizing event								
Quartz-1 in volcanite			Quartz-1 in black shale			Dolomite-2 in black shale		
Inclusions	T _h (°C)	T _{mi} (°C)	Inclusions	T _h (°C)	T _{mi} (°C)	Inclusions	T _h (°C)	T _{mi} (°C)
Inc. 38	196.28	-6.27	–	–	–	Inc. 38	179.50	-21.96
Inc. 39	185.46	-6.82	–	–	–	Inc. 39	159.11	-16.39
Inc. 40	185.10	-5.74	–	–	–	Inc. 40	166.53	-18.78
Inc. 41	183.87	-6.04	–	–	–	Inc. 41	155.39	-25.54
Inc. 42	192.35	-7.62	–	–	–	Inc. 42	154.94	-23.16
Inc. 43	159.10	-7.30	–	–	–	Inc. 43	169.36	-24.68
Inc. 44	158.72	-7.27	–	–	–	Inc. 44	183.31	-17.48
–	–	–	–	–	–	Inc. 45	181.03	-16.01
–	–	–	–	–	–	Inc. 46	175.55	-17.36

See text for the abbreviations

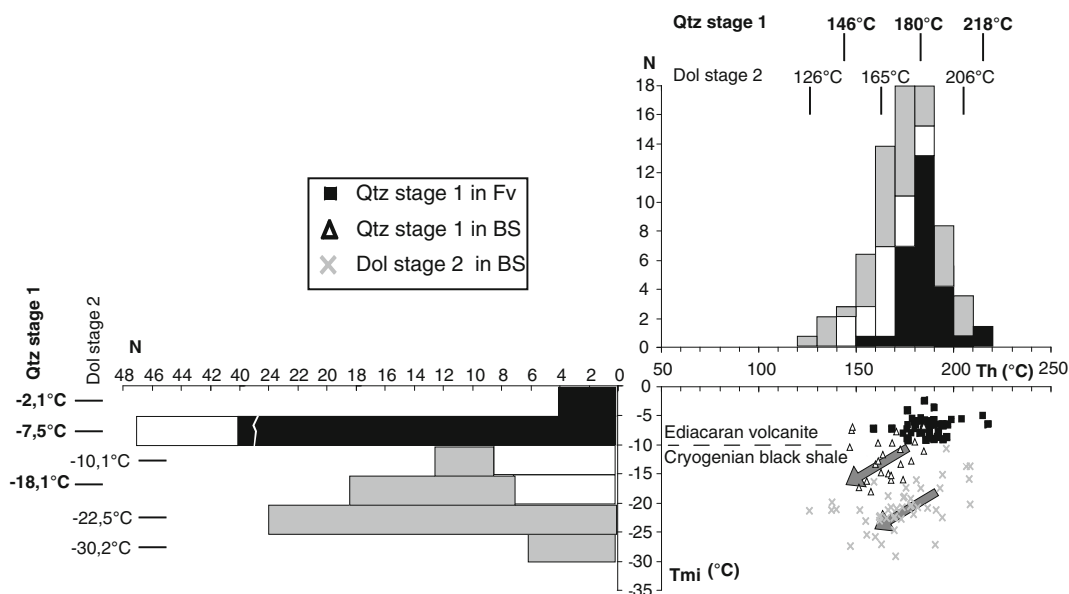
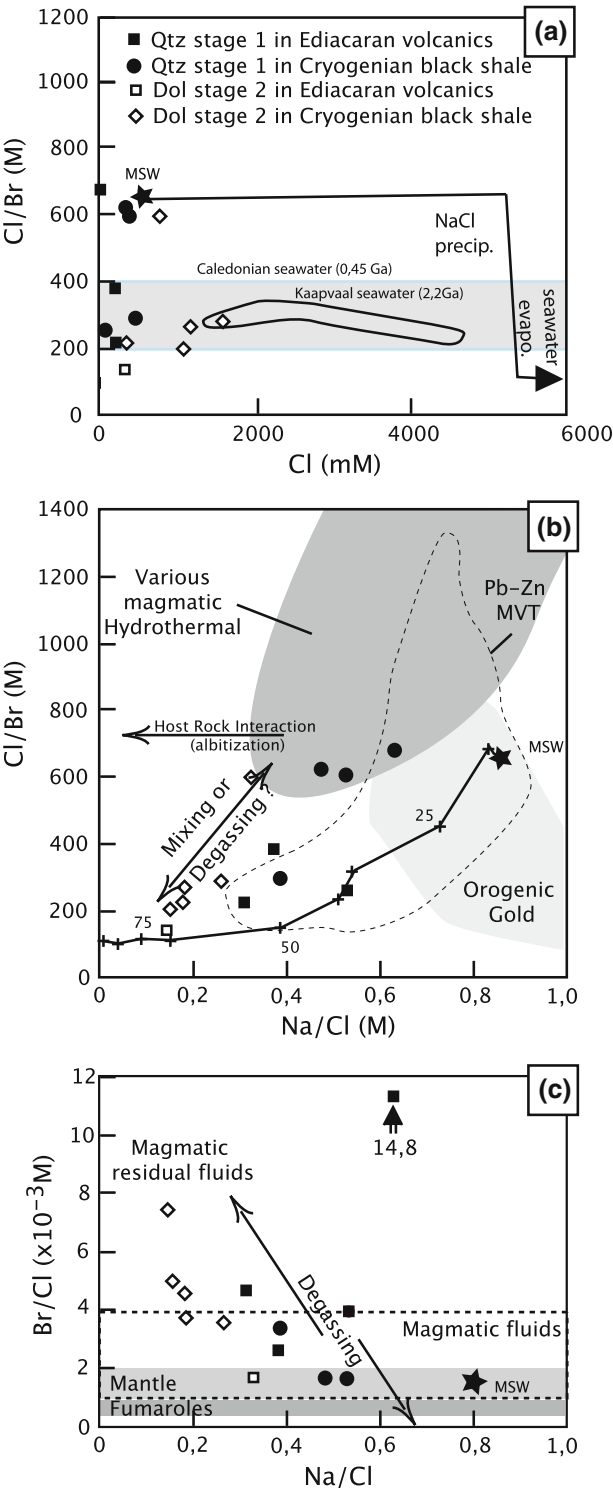


Fig. 3 Homogenization temperature (T_h) versus melting temperature (T_{mi}) diagram for fluid inclusions from the Imiter epithermal silver deposit. Arrows represent inferred fluid evolution and related degassing process

Fig. 4 Halogen ratios for fluid-inclusion leachates from the Imiter Ag–Hg deposit. **a** $(\text{Cl}/\text{Br})_{\text{mol}}$ versus Cl_{mmol} . Data for Kaapvaal Proterozoic and Caledonian seawater are from Kendrick et al. (2005), Foriel et al. (2004), and Spear et al. (2014). *Black line* shows seawater evaporation trend; filled star is modern seawater composition (MSW) (Fontes and Matray 1993). **b** $(\text{Cl}/\text{Br})_{\text{mol}}$ versus $(\text{Na}/\text{Cl})_{\text{mol}}$. Various magmatic and hydrothermal fields and orogenic gold fields are shown for comparison (modified from Hofstra and Landis 2012). In this plot, both mixing and degassing processes can explain the observed data distribution. **c** $(\text{Br}/\text{Cl})_{\text{mol}}$ versus $(\text{Na}/\text{Cl})_{\text{mol}}$. Fields for magmatic fluids, mantle, and fumaroles are from Kendrick et al. (2001, 2005). Distribution of data suggests predominance of degassing from primary magmatic fluids to magmatic-hydrothermal fluids



8 Fluid Inclusion Leachate Compositions

Na–K–Cl–Br–Li–F–SO₄ compositions of fluid inclusions hosted in Qz-1 and Dol-2 from both mineralized and barren veins were determined on the same mineral wafers as those used for microthermometric measurements. The recorded compositions are presented in Table 2 and plotted in Fig. 4.

Overall, the leachate compositions are dominated by Na, Cl, K, and SO₄ ± Br ± Li ± (Table 2; Fig. 4a–c). Concentrations of Cl, Br, Na, K, and SO₄ show relative enrichment from Qz-1 to Dol-2. Conversely, F and Li contents decrease gradually with paragenetic stage from early to late. It is noteworthy that the leachate composition of Qz-1 samples from veins hosted in the Cryogenian black shale display higher Na/Br and K/Br molar ratios than those samples hosted in Ediacaran volcanic rocks. This pattern is attributed to a host-rock chemical control and hence suggests the importance of water-rock interactions during silver mineralization.

In the Cl/Br versus Cl diagram, the halogen compositions of Qz-1 and Dol-2 plot in two distinct fields (Fig. 4a). The field for Qz-1 fluid inclusions shows a vertical distribution in two groups, both having low Cl concentrations. The first group has a Cl/Br ratio comparable to those inferred for Archean and Devonian seawater (Foriel et al. 2004; Kendrick et al. 2005; Spear et al. 2014), whereas data for the second group are close to the Cl/Br ratio for modern seawater. Data for Dol-2 display a level distribution with a lower Cl/Br ratio and increasing chlorine concentration. Br/Cl ratios of fluids trapped both in Qz-1 and Dol-2 vary from 1 to 14, and are consistent with magmatic brine compositions (Fig. 4c; Déruelle et al. 1992; Johnson et al. 2000), bounded at lower limits by mantle values of 1–2 (Kendrick et al. 2001, 2005). In the Cl/Br versus Na/Cl diagram (Fig. 4c), the Qz-1 and Dol-2 halogen compositions show Na

enrichment attributed to either water/rock interaction with clays, or leaching of sodic plagioclase from footwall rocks. Both processes produced a similar distribution connecting the magmatic fluid field and the mean sea water (MSW) evaporation line. Intersections with the MSW evaporation line and the epithermal silver event occur up to 50 % evaporation, which represents the maximum evaporation reported for evolved brines (as in MVT deposits; Kesle et al. 1996; Tritlla et al. 2001). Two main processes could explain these distributions (1) mixing between magmatic and evaporated meteoric water, and (2) a degassing process.

9 Mineral Assemblage Thermometry

Electron microprobe analyses of chlorite from the main veins indicate a wide spectrum of compositions from brunsvigite to picnochlorite (Baroudi 1992; Bajja 1998; Cheilietz et al. 2002; present study). Application of the chlorite geothermometer of Cathelineau (1988) suggests temperatures of equilibration of 266 ± 15 – 304 ± 15 °C (mean 278 ± 15 °C; Fig. 5). Moreover, the mineral assemblage pyrite–proustite–argentite–realgar indicates equilibrium temperatures in the range of 350–230 °C (pyrite/pyrrhotite and silver sulphides in coexisting domains; see paragenetic sequence in Fig. 2), corresponding to sulphur fugacities of 10^{-8} – 10^{-15} (Fig. 6; see Barton and Skinner 1967). The identification of dodecahedral crystals of acanthite (Levresse 2001) establishes a lower temperature limit for crystallization of 173 °C for the silver in Dol-2 stage (Kracek 1946). For the temperature range of Qtz-1 (350–230 °C), the oxygen fugacity is estimated at 10^{-30} – 10^{-39} (D'Amore and Panichi 1980), and together with the lack of abundant Ag sulphides suggests low oxygen and sulphur activities during the major silver mineralizing event (Levresse 2001).

Table 2 Chemical composition of typical fluid inclusions of silver epithermal stages from Imiter Ag–Hg deposit

Sample	Host rock	Level	Th _{L,V} range	T _m range	CO ₂ /CH ₄ /N ₂	F	Cl	Br	SO ₄	Na	K	Li	Na/Br	Cl/Br	K/Cl	Na/Cl
Shaft-number		masl	°C	°C	Mean mol%	mol%										
IMIII-9958	BS	1325	181/342	-7.3/-1.7	26/68/21	26	4396	14	99	1430	445	19	347.57	692.9	0.09	0.50
IMIV-9937	BS	1320	151/323	-13.5/-0.1	nd	23	3197	57	65	1000	453	11	609.78	1264	0.13	0.48
<i>ESE-Qrz2</i>																
IMIII-9959	VF	1483	156/211	-7.7/-2.5	nd	24	807	27	46	330	95	10	424.81	673.7	0.11	0.63
IMIII-9960	VF	1483	158/204	-6.7/-2.1	00/66/44	20	7134	75	167	1440	486	16	66.82	214.7	0.06	0.31
IMIII-9960	VF	1483	156/218	-9.2/-2.8	36/64/0	13	6832	40	12,201	1650	493	165	142.31	382.1	0.07	0.37
IMI-0501	BS	1400	148/162	-12.7/-7.1	00/72/28	0	12,835	48	536	4390	689	24	315.91	599	0.05	0.53
IMIII-9954	BS	1335	147/185	-8.1/-3.4	nd	13	15,263	119	92	3830	972	110	111.87	289.1	0.06	0.39
IMIII-0004	BS	1325	147/180	-18.1/-9.5	nd	31	11,634	42	402	3590	1410	67	294.99	619.9	0.11	0.48
IMIII-0022	BS	1320	154/185	-8.6/-4.2	nd	16	2323	21	534	800	369	21	134.33	253	0.14	0.53
<i>ESE-Dol</i>																
IMIII-9960	VF	1483	145/197	-18.8/-11.5	nd	0	11,239	187	270	1040	277	80	19.28	135.1	0.02	0.14
IMI-0501	BS	1400	126/182	-22.8/-13.7	nd	0	26,355	100	1099	5550	954	15	192.90	594	0.03	0.32
IMIII-0022	BS	1320	141/224	-13.1/-10.1	nd	0	11,523	119	300	1333	409	10	38.93	218.3	0.03	0.18
IMIII-9957	BS	1325	149/171	-30.2/-12.8	nd	0	37,796	429	429	3720	1654	59	30.14	198.6	0.04	0.15
IMIII-9958	BS	1325	145/206	-28.4/-18.6	nd	20	56,010	447	17,844	9480	2322	47	73.71	282.4	0.04	0.26
IMIII-0005	BS	1325	152/163	-23.7/-12.1	nd	0	41,261	354	1099	4890	1592	58	48.01	262.7	0.04	0.18

Abbreviations BS black shale; nd not determined; VF volcanic formation

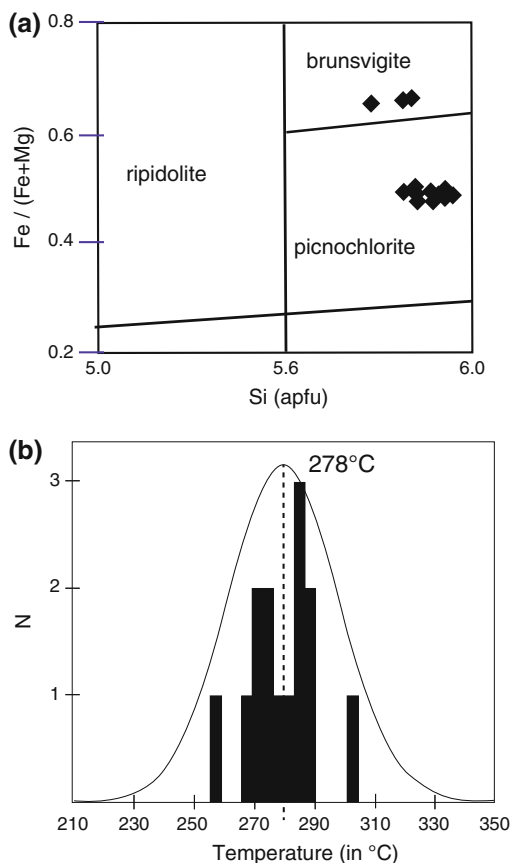


Fig. 5 **a** Plot of Fe/(Fe + Mg) ratio in chlorite versus number of Si atoms for samples from the base-metal-bearing quartz veins. Classification scheme after Bayliss (1985). **b** Calculated temperatures for chlorite crystallization, based on the chlorite geothermometer of Cathelineau (1988). N, number of analyses

10 C–O–S Isotopic Compositions

Sulphides and gangue minerals from the early uneconomic, non-argentiferous, base-metal (BSM) stage and the following ESE-Qz and ESE-Dol stages related to the main epithermal silver mineralization, and pyrite from the Cryogenian black shales, have been analyzed for carbon, oxygen, and sulphur isotopic compositions by previous workers (Pašava 1994; Levresse et al. 2004).

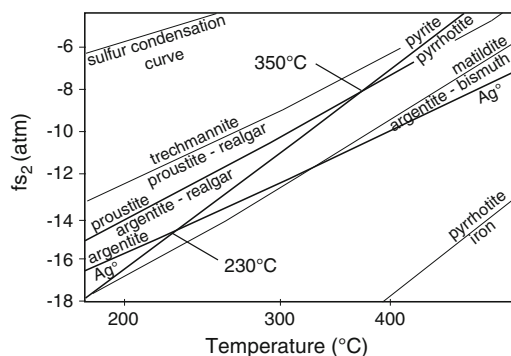


Fig. 6 Phase equilibria in Ag–Hg–Fe–Bi–S system as a function of temperature and sulphur fugacity during ESE-Qz—epithermal silver stage (modified from Barton and Skinner 1967). Noted are 230 and 350 °C isotherms that represent range of temperatures of Imiter epithermal system, where pyrite and silver sulphides coexist (see Fig. 2)

Pyrite separates from the black shales have $\delta^{34}S_{CDT}$ values of -38.5 ± 2.0 to -37.4 ± 2.0 ‰. In contrast, pyrite separates from the BSM stage show $\delta^{34}S$ values that range from -7.4 ± 1.0 to -2.0 ± 0.8 ‰. Sulphide separates (i.e., pyrite, galena, sphalerite, chalcocopyrite) from the ESE-Qz and ESE-Dol stages show a wide spread in sulphur isotopic compositions, with $\delta^{34}S_{CDT}$ ratios for the ESE-Qz stage ranging from -11.9 ± 0.8 to -2.4 ± 0.8 ‰ (avg -8.5 ± 2.5 ‰), whereas those determined for following ESE-Dol stage oscillate from -27.7 ± 0.4 to -1.8 ± 1.2 ‰ (avg -13 ± 8.1 ‰). The isotopically lowest value ($\delta^{34}S = -27.7 \pm 0.4$ ‰) was measured on cinabar that is paragenetically the latest mineral phase (Levresse et al. 2004).

Carbon and oxygen isotopic compositions of dolomite separates (i.e., Dol-2) from both barren and mineralized orebodies display overlapping $\delta^{13}C$ and $\delta^{18}O$ values. Carbon isotope values ($\delta^{13}C_{PDB}$) range from -10.5 to -2.2 ‰, with most data between -11 to -8 ‰, whereas oxygen isotope values ($\delta^{18}O_{PDB}$) vary from -13.4 to -0.1 ‰ (Pašava 1994).

11 Os and He Isotopic Compositions

Initial age-corrected Os isotope ratios [$(^{187}\text{Os}/^{188}\text{Os})_{550\text{Ma}}$] determined for the ESE-Qz and ESE-Dol stages range from 0.142 to 0.197 and record a predominant mantle source for osmium in the Imiter ores (Levresse et al. 2004). These ratios are slightly higher than the average mantle value of about 0.12 at ca. 550 Ma, which probably reflects a minor contribution (<10 vol. %) from a crustal component, possibly the Cryogenian black shales. $^3\text{He}/^4\text{He}$ ratios measured on quartz, dolomite, galena, and pyrrhotite from the ESE-Qz and ESE-Dol stages vary from 0.77 to 1.85. ^{20}Ne concentrations are indistinguishable from the blank, demonstrating an extremely low Ne content and lack of significant contribution from atmospheric gases. $^3\text{He}/^4\text{He}$ ratios show excesses of ^3He relative to typical crustal fluids, thus strongly suggesting a contribution of mantle volatiles to fluids that

were trapped in the analyzed minerals (Levresse et al. 2004).

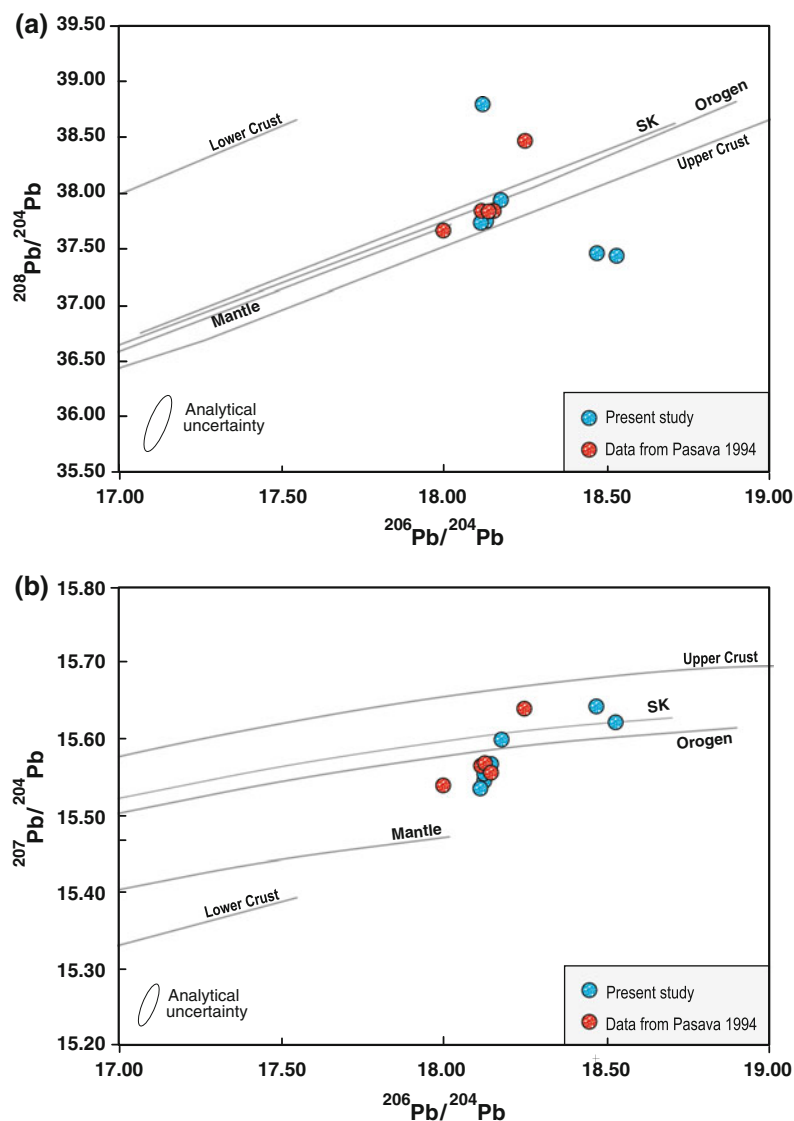
12 Lead Isotopic Compositions

New lead isotope measurements performed on six galena separates from the ESE-Qz and ESE-Dol stages are presented in Table 3 and plotted in Fig. 7. Lead isotope ratios for galena separates range from 17.995 to 18.523 for $^{206}\text{Pb}/^{204}\text{Pb}$, 15.532–15.673 for $^{207}\text{Pb}/^{204}\text{Pb}$, and 37.462–38.797 for $^{208}\text{Pb}/^{204}\text{Pb}$. These compositions, which overlap the values reported by Pašava (1994), plot between the upper crust and mantle growth curves and resemble the orogen reservoir of Zartman and Doe (1981). Good reproducibility of the data indicates that the observed scatter does not represent an artefact of analytical error and/or mass fractionation bias. Instead, we interpret the roughly linear array as a binary mixing line, suggestive of a mixing of

Table 3 Sulphur and lead isotopic compositions of galena separates from Imiter Ag–Hg deposit

Samples	Mineral	$\delta^{34}\text{S}_{\text{CDT}}$ (‰)	$^{206}\text{Pb}/^{204}\text{Pb}$	$^{207}\text{Pb}/^{204}\text{Pb}$	$^{208}\text{Pb}/^{204}\text{Pb}$
I 1.1	Galena	−7.8	18.112	15.559	37.810
I 1.2	Chalcopyrite	−7.3	–	–	–
I 2.2	Pyrite	−6.2	–	–	–
I 3.1	Pyrite	−5.7	–	–	–
I 4.2	Galena	–	17.995	15.536	37.661
I 7.1	Galena	−5.8	–	–	–
I 8.1	Galena	−6.2	–	–	–
I 8.1 QCD	Galena	−5.9	–	–	–
I10.2	Galena	–	18.136	15.553	37.826
I 11.2	Galena	−5.6	–	–	–
I12.1	Galena	–	18.123	15.565	37.840
I 13.1	Galena	−5.1	–	–	–
I 14.1	Galena	−8.3	–	–	–
L 1.2	Galena	−7.2	18.111	15.561	37.823
L1 5	Galena	–	18.244	15.636	38.462

Fig. 7 Lead isotopic compositions of galena separates from Imiter Ag–Hg deposit, plotted on **a** $^{208}\text{Pb}/^{204}\text{Pb}$ versus $^{206}\text{Pb}/^{204}\text{Pb}$ and **b** $^{207}\text{Pb}/^{204}\text{Pb}$ versus $^{206}\text{Pb}/^{204}\text{Pb}$ diagrams. Evolution curves of Stacey and Kramers (1975) labeled SK and those for Upper Crust and Orogen (Zartman and Doe 1981) are shown for reference



lead from mantle and crustal reservoirs during leaching and fluid transport, consistent with the sulphur isotope and He isotope data described above.

13 Discussion

Mineralogical, textural, and geochemical attributes of the Imiter silver vein mineralization clearly point to an epithermal deposit type (Figs. 1 and 2). Diagnostic features in support of this classification include the presence of

adularia (Borisenko et al. 2013), occurrence of large open structures filled by ore and gangue minerals, and widespread development of vuggy quartz, all of which are characteristic of a shallow and brittle environment. An epithermal model for Imiter has been proposed by previous workers (Levresse 2001; Cheilletz et al. 2002; Levresse et al. 2004; Burniaux and Williams-Jones 2006), and since then has been extended to most, if not all, of the Ag-rich deposits in the Anti-Atlas Mountains (Ennaciri et al. 1997; Essaraj et al. 1999, 2005; Marcoux and Wadjinny 2005).

Paragenetic studies indicate that the history of the Imiter mineralizing system involved two main contrasting hydrothermal events (Fig. 1) that occurred under two distinct mainly extensive tectonic events (Ouguir et al. 1994; Tuduri et al. 2005). These two stress fields are similar to those that gave rise to the late Neoproterozoic Bou Madine epithermal Au–Ag–Pb–Zn deposit described in this volume by Bouabdellah and Levresse. However, owing to the lack of robust absolute ages for each mineralizing event at Imiter, it is unclear whether these two hydrothermal events involved a single mineralizing fluid or two chronologically separate fluids. The confinement of silver mineralization to the transcrustal Imiter fault zone suggests that silver-bearing hydrothermal fluids were channeled through fractured rocks, en route to depositional sites in veins hosted by overlying black shales and along the contact between the upper and lower lithostratigraphic units of the Neoproterozoic succession.

Fluid inclusion data show the existence of two distinct fluid inclusion populations having similar temperature ranges but contrasting salinities (Table 1, Figs. 3 and 4). A consistent trend is apparent towards slightly lower temperatures but higher salinities with advancing paragenetic stage. The early mineralizing fluids related to the ESE-Qz stage had a mean temperature of ~ 180 °C and corresponding salinity of ~ 10 wt % NaCl equiv, whereas the subsequent ESE-Dol stage fluids had a lower mean temperature of ~ 165 °C but with a substantially higher mean salinity of ~ 24 wt% NaCl equiv. Similarly, the fluid compositions evolved by relative decreases in Na^+ , K^+ , and SO_4 and a concomitant increase in Ca^{2+} with time (i.e., from Qz-1 to Dol-2 stages).

Estimates of minimum trapping pressure are in the range of 1.1–0.9 kbar for the mineralizing fluid responsible for Imiter silver mineralization. Within this range of pressures, as well as temperatures (206–126 °C) and salinities (0–15 wt% NaCl equiv), thermodynamic restrictions preclude boiling of the fluid (Hass 1976). The absence of platy calcite (Simmons et al. 2005), and also of co-existing vapor-rich and liquid-rich

inclusions that homogenize over the same temperature range (see Roedder 1984), indicate again that fluid boiling did not occur during trapping of these fluid inclusions.

Measured Br/Cl molar ratios of fluids related to the ESE-Qz and ESE-Dol stages are consistent with the involvement of magmatically derived fluid components (Fig. 4). Moreover, elements such F and Li that are considered reliable proxies of magmatic degassing (Deering et al. 2012; Vlastélic et al. 2013; Chen et al. 2015), have higher concentrations in Qz-1 than in Dol-2. We thus propose that degassing of CO_2 and SO_2 during epithermal mineralization (e.g., Bendežú et al. 2008 and references therein) led to a decrease of local redox potential and a pH increase, which together with other ore controls such as decreasing temperature and lowering of f_{O_2} by fluid interaction with the organic-rich black shales, resulted in deposition of massive Hg–Ag amalgam instead of separate Ag and Hg sulphide minerals (Borisenko et al. 2013). The high water/rock ratios that prevailed during ore deposition would have developed a large hydrothermal alteration halo around and adjacent to the Imiter mineralized structures, and within the Cryogenian black shales as well.

It is noteworthy that halogen contents of fluids generated during open-system degassing can be highly variable (Villemant and Boudon 1999; Aiuppa et al. 2009) with concentrations being higher in the first extracted fluid fractions than in the last ones. Conversely, fluids produced during closed-system evolution commonly show nearly constant halogen contents but much lower Br abundances; Cl contents, in contrast, remain similar to those resulting from open-system degassing (Villemant and Boudon 1999). Involvement of ore-forming brines in which high salinities are derived either directly from seawater evaporation or from exchange reactions with sedimentary evaporite strata (i.e., halite dissolution) is precluded, because the expected increase in the abundances of salt (KCl_2 , CaCl_2 , MgCl_2) and sulphate in the residual fluids (Horita et al. 2002; Brennan et al. 2004; Foriel et al. 2004; Kendrick et al. 2005; Spear et al. 2014) are not observed in the Imiter fluid inclusions.

In contrast to this predicted trend, measured Na/Cl, K/Cl, and SO₄/Cl ratios for the fluid inclusions show a systematic decrease from early to late mineralizing stages. Moreover, the negative correlation between SO₄ abundances and Br/Cl ratios indicates that seawater is unlikely to be the predominant source of the ore-forming brine. In our model for the Imiter Ag–Hg deposit, the degassing process explains the physico-chemical evolution of the epithermal system without the necessity of invoking a mixing with basinal brines. More importantly, at the time of ore formation the closest basinal brine sources were 80 km from the mineralized area (Álvaro 2014). Also, the first sedimentary record known in the Imiter deposit area is from the Middle Cambrian (Piqué et al. 1999; Álvaro 2014), which is 30 m.y. later than the Neoproterozoic silver mineralizing event.

In conclusion, fluid inclusion data together with halogen compositions and sulphur and lead isotope data are consistent with the involvement of a magmatic component in the Imiter hydrothermal system. Indeed, the large spread in sulphur isotopic values for the ESE mineralizing event is interpreted as resulting from preferential degassing of SO₂ in ascending fluids and mixing between magmatic and country rock reservoirs. Moreover, the linearity displayed by lead isotopic compositions is suggestive of a mixing of lead from mantle and crustal reservoirs during leaching and fluid transport.

Continuous input of magmatically equilibrated fluids into the hydrothermal system is supported by the observed increases in Hg concentrations of the Hg–Ag amalgam from the Qz-1 to Dol-2 stages (10–30 vol.% and 20–40 vol.%; respectively). Calculated $\delta^{18}\text{O}_{\text{H}_2\text{O}}$ values of the ore-forming fluid, using the dolomite–H₂O fractionation factor of Zheng (1999) and the average temperature of 165 °C inferred from fluid inclusion data, are in the range of 6.3–19.6 ‰ V-SMOW. These values are consistent with a mixture of magmatic and metamorphic fluids. Interaction of the mineralizing fluids with the enclosing Neoproterozoic organic-rich black shale host rocks could have produced a large volume of reduced and low-pH

fluids that were capable of transporting and precipitating Ag and associated base metals, as well as providing a source of carbon for the late ore-bearing carbonate gangue.

The light carbon isotopic signatures of Dol-2 separates (Pašava 1994) and abundance of CH₄- and N₂-rich fluid inclusions provide further support for involvement of the black shales as reactive host rocks during the mineralizing process. Such water/rock interaction may have contributed to thermochemical reduction and associated precipitation of Ag-bearing sulphide minerals. Mass-balance calculations suggest, however, that the contribution of components from the black shales to the Imiter hydrothermal system was rather limited (i.e., <10 vol.%; Levresse et al. 2004). Moreover, ¹⁸⁷Os/¹⁸⁸Os and ³He/⁴He data, together with lead isotope data, are consistent with various degrees of mixing between mantle and crustal sources along the fluid flow path.

Integrated results from geological, structural, and geochemical studies (Fig. 8) indicate that hydrothermal fluids were channeled from a deep source to a shallow hydrothermal system by the crustal-scale Imiter fault zone. In our model, these magmatic-related fluids percolated through the Cryogenian black shales, and were progressively buffered and acquired a different geochemical signature compared to the initial magmatically derived fluids. This concept involves different pulses of epithermal mineralizing fluids and a wide range of water/rock ratios, in particular for CO₃, Ca, Mg, Pb, and S that were leached from the Cryogenian black shales and/or rocks in the lower basement. The proposed magmatic input during the epithermal silver mineralizing stages added to the fluid confinement within the Cryogenian black shales (favored by the Ediacaran volcanic seal), and is considered the principal reason for the richness of the Imiter deposit and its continuity at depth (at least 900 m at present).

It is also noteworthy that the He and Os isotope data are inconsistent with the supergene model for silver enrichment as initially proposed by Guillou et al. (1988), Leistel and Qadrouci (1991), and Baroudi et al. (1999).

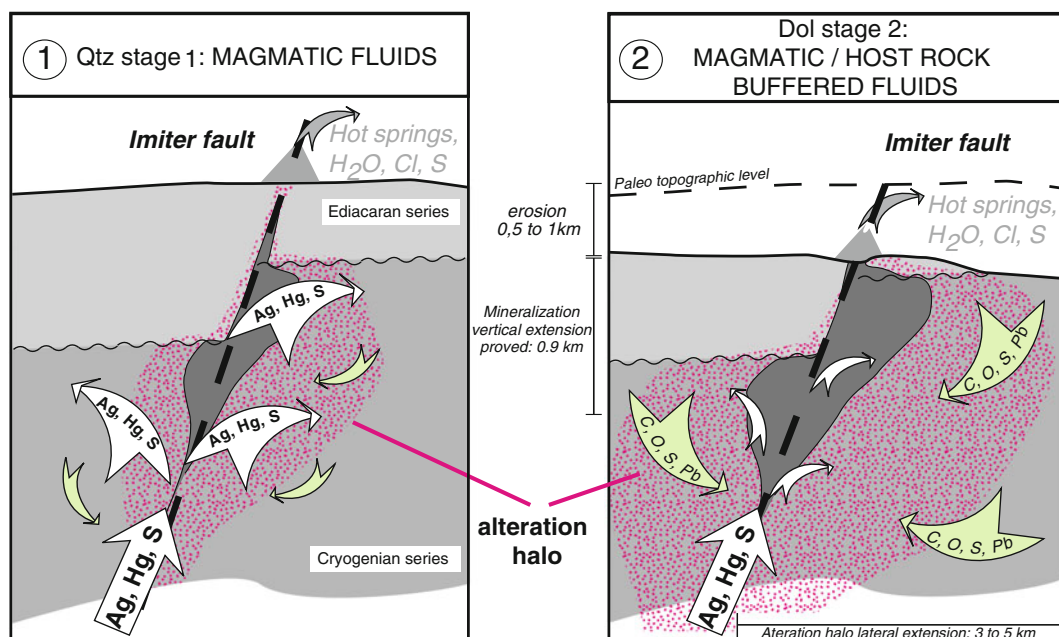


Fig. 8 Genetic model for Imiter Ag–Hg deposit. 1 ESE quartz stage 1 event. 2 ESE dolomite stage 2 event. Simplified geological cross sections are drawn from B3 Hill transect (modified from Levresse 2001). Model

illustrates evolution of the silver epithermal system particularly the importance of magmatic fluid degassing, the Ediacaran volcanic seal, and increasing water-rock interaction from stage ESE Qz-1 to ESE Dol-2 stages

14 Conclusions

The giant Imiter deposit is a prime example of major Ag–Hg mineralization linked with Ediacaran volcanism dated at ca. 550 Ma. To build such a giant metal concentration, three essential ingredients should have been available together (Fig. 8), including: (1) a powerful and long-lasting magmatic source connected by major tectonic structures to one or more asthenosphere reservoirs; (2) reactive and highly permeable, metamorphosed and foliated organic-rich host rocks that facilitated the transmission of fluids and increased the surface area of fluid/rock interactions, in addition to generating the reducing conditions necessary for metal precipitation; and (3) overlying cap rocks that prevented escape of the hydrothermal fluids to the surface, instead forcing these fluids to an increased residence time and dissemination within the most receptive formation (lithological trap).

The striking feature of the Imiter Ag–Hg deposit is the duration and chemical evolution of the causative epithermal activity. With advancing paragenetic sequence, the epithermal system was self-regulating, whereas the interaction between magmatically derived fluids and host rocks became predominant. This inferred process may explain the transition from quartz-dominant to dolomite-dominant Ag–Hg mineralization through the paragenetic sequence. In such a low-sulphidation metallogenic model, the involvement of meteoric waters is not a prerequisite to explain metal precipitation, nor is supergene enrichment needed to obtain the very high volume and grade of the ores. Magmatic degassing into the hydrothermal system, coupled with fluid/rock interactions, ultimately led to development of a local decrease in redox potential and an increase in pH, which coupled with other ore controls (e.g., decreasing fluid temperature), triggered deposition of massive Hg–Ag amalgam instead of Hg and Ag sulphide minerals.

Acknowledgments Special thanks to Marina Vega and Teresa Soledad Medina Malagón for assistance at the CGEO laboratory. This study was financed by UNAM-PAPIIT project IN110912 and CONACYT projects 81584 and 80142. We also thank John Slack for his constructive review, which led to numerous improvements in the quality and clarity of the text.

References

- Aiuppa A, Baker DR, Webster JD (2009) Halogens in volcanic systems. *Chem Geol* 263:1–18
- Álvarez JJ (2014) Rift, pull-apart rift and continental drift crossword puzzles across the lower-middle Cambrian transition of Iberia and Morocco. *GFF* 136:2–5
- Álvarez JJ, Beallido F, Gasquet D, Pereira MF, Quesada C, Sanchez-García T (2014). Diachronism in the late Neoproterozoic–Cambrian arc-rift transition of North Gondwana: A comparison of Morocco and the Iberian Ossa-Morena Zone. *J Afr Earth Sci* 98:113–132
- Bajja A (1998) Volcanisme syn à post orogénique du Néoprotérozoïque de l'Anti-Atlas: implications pétrogénétiques et géodynamique. Thèse d'Etat Es-sciences, Univer Chouaib Doukkali, El Jadida, Maroc, 215 pp
- Banks DA, Giuliani G, Yardley BWD, Cheilletz A (2000) Emerald mineralisation in Colombia: fluid chemistry and the role of brine mixing. *Mineralium Deposita* 35:699–713
- Baroudi Z (1992) Contribution à l'étude métallogénique des minéralisations mercuro-argentifères du district d'Imiter Saghro Oriental, Anti-Atlas, Maroc. Thèse, University of Marrakech, 188 pp
- Baroudi Z, Beraouz H, Rahimi A, Saquaque A, Chouhaidi M (1999) Minéralisations polymétalliques argentifères d'Imiter Jbel Saghro, Anti-Atlas, Maroc: minéralogie, évolution des fluides minéralisateurs et mécanismes de dépôts. *Chronique Recherche Minière* 536–537:91–111
- Barton PB Jr, Skinner BJ (1967) Sulfide mineral stabilities. In: Barnes HL (ed) *Geochemistry of hydrothermal ore deposits*. Holt, Reinhart & Winston Inc, New York, pp 236–333
- Bayliss P (1985) Nomenclature of the trioctahedral chlorites. *Can Mineral* 13:178–180
- Bendezú R, Page L, Spikings R, Pecsckay Z, Fontboté L (2008) New $^{40}\text{Ar}/^{39}\text{Ar}$ alunite ages from the Colquijirca district, Peru: evidence of a long period of magmatic SO_2 degassing during formation of epithermal Au-Ag and Cordilleran polymetallic ores. *Miner Deposita* 43:777–789
- Borisenko AS, Borovikov AA, Pavlova GG, Kalinin YuA, Nevolko PA, Lebedev VI, Maacha L, Kostin AV (2013) Formation conditions of Hg-silver deposition at the Imiter deposit (Anti-Atlas, Morocco). In: Johnsson E et al (eds) *Mineral deposit research for a high-tech world*. Proceedings of 12th biennial SGA meeting, Uppsala, Sweden 3:1243–1246
- Brennan ST, Lowenstein TK, Horita J (2004) Seawater chemistry and the advent of biocalcification. *Geology* 32:473–476
- Burniaux P, Williams-Jones AE (2006) Controls of silver-mercury mineralization at Imiter, Morocco. *Geol Assoc Canada Pgm Abs* 31:22
- Cathelineau M (1988) Cation site occupancy in chlorites and illites as a function of temperature. *Clay Miner* 23:471–485
- Cheilletz A, Levresse G, Gasquet D, Azizi Samir MR, Zyadi R, Archibald DA (2002) The Imiter epithermal deposit (Morocco): new petrographic, microtectonic and geochronological data. Importance of the Precambrian-Cambrian transition for major precious metals deposits in the Anti-Atlas. *Miner Deposita* 37:772–781
- Chen Z, Xu Y, Zheng K (2015) Geochemistry of potential high temperature geothermal resources in Kangding, Sichuan, China. In: *Proceedings of world geothermal congress*, Melbourne, Australia, pp 1–7
- D'Amore F, Panichi G (1980) Evaluation of deep temperatures of hydrothermal systems by a new gas geothermometer. *Geochim Cosmochim Acta* 44:549–556
- Deering CD, Horton TW, Gravley DM, Cole JW (2012) Hornblende, cummingtonite, and biotite hydrogen isotopes: direct evidence of slab-derived fluid flux in silicic magmas of the Taupo volcanic zone, New Zealand. *J Volcanol Geoth Res* 233–234:27–36
- Déruelle B, Dreibus G, Jambon A (1992) Iodine abundances in oceanic basalts: implications for Earth dynamics. *Earth Planet Sci Lett* 108:217–227
- Dubessy J, Buschaert S, Lamb W, Pironon J, Thierry R (2001) Methane-bearing aqueous fluid inclusions: Raman analysis, thermodynamic modelling and application to petroleum basins *Chem Geol* 173:193–205
- Ducrot J, Lancelot JR (1977) Problème de la limite Précambrien-Cambrien: étude radiochronologique par méthode U-Pb sur zircon du Jbel Bobo (Anti-Atlas marocain). *Can J Earth Sci* 14:2771–2777
- Ennaciri A, Barbanson L, Touray JC (1997) Brine inclusions from the Co-As-(Au) Bou Azzer district, Anti-Atlas Mountains, Morocco. *Econ Geol* 92:360–367
- Ennih N, Liégeois JP (2001) The Moroccan Anti-Atlas: the West African craton passive margin with limited Pan-African activity, implications for the northern limit of the craton. *Precamb Res* 112:289–302
- Essaraj S (1999) Circulations de fluides associées aux minéralisations argentifères de l'Anti-Atlas central: exemples des gisements de Zgounder (Ag-Hg) et Bou-Azzer (Co-Ni-As-Au-Ag). Université Cadi-Ayyad, Marrakech, Maroc, Thèse d'Etat 358 pp
- Essaraj S, Boiron MC, Cathelineau M, Banks DA, Benharref M (2005) Penetration of surface-evaporated brines into the Proterozoic basement and deposition of Co and Ag at Bou-Azzer (Morocco):

- evidence from fluid inclusions. *J Afr Earth Sci* 41:25–39
- Fekkak A, Pouclet A, Ouguir H, Ouazzani H, Badra L, Gasquet D (2001) Géochimie et signification géotectonique des volcanites du Cryogénien inférieur du Saghro (Anti-Atlas oriental, Maroc). *Geodinam Acta* 14:373–385
- Fontes JC, Matray JM (1993) Geochemistry and origin of formation brines from the Paris Basin, France 1. Brines associated with Triassic salts. *Chem Geol* 109:149–175
- Foriel J, Philippot P, Rey P, Somogyi A, Banks DA, Menez B (2004) Biological control of Cl/Br and low sulfate concentration in a 3.5-Gyr-old seawater from North Pole, Western Australia. *Earth Planet Sci Lett* 228:451–463
- Gasquet D, Chevremont P, Baudin T, Chalot-Prat C, Guerrot C, Cocherie A, Roger J, Hassenforder B, Cheilletz A (2004) Polycyclic magmatism in the Tagragra and Kerdous-Tafeltast inliers (western Anti-Atlas, Morocco). *J Afr Earth Sci* 39:267–275
- Gasquet D, Levresse G, Cheilletz A, Deloule E, Azizi Samir MR, Zyadi R (2005) Contribution to a geodynamic reconstruction of the Anti-Atlas (Morocco) during Pan African times with the emphasis on inversion tectonics and metallogenetic activity at the Precambrian-Cambrian transition. *Precambr Res* 140:157–182
- Guillou J-J, Monthel J, Picot P, Pillard F, Protas J, Samama J-C (1985) L'imitérite, Ag_2HgS_2 , nouvelle espèce minérale; propriétés et structure cristalline. *Bulletin de Mineralogie* 108:457–464
- Guillou JJ, Monthel J, Samama JC, Tijani A (1988) Morphologie et chronologie relative des associations minérales du gisement mercuro-argentifère d'Imiter (Anti-Atlas, Maroc). *Notes Mémoires Service Géologique Maroc* 334:215–228
- Haas JL (1971) The effect of salinity on the maximum thermal gradient of a hydrothermal system at hydrostatic pressure. *Econ Geol* 66:940–946
- Hey MH (1954) A new review of the chlorites. *Min Mag* 30:227–292
- Hofstra AH, Landis GP (2012) Ore genesis constraints on the Idaho cobalt belt from fluid inclusion gas, noble gas isotope, and ion ratio analyses. *Econ Geol* 107:1189–1205
- Horita J, Zimmermann H, Holland HD (2002) Chemical evolution of seawater during the Phanerozoic: implications from the record of marine evaporates. *Geochim Cosmochim Acta* 66:3733–3756
- Johnson L, Burgess R, Turner G, Milledge JH, Harris JW (2000) Noble gas and halogen geochemistry of mantle fluids: comparison of African and Canadian diamonds. *Geochim Cosmochim Acta* 64:717–732
- Katrivanos FC (2015) Silver. U.S. Geological Survey 2012 Minerals Yearbook. <http://minerals.usgs.gov/minerals/pubs/commodity/silver/myb1-2012-silver.pdf>
- Kendrick MA, Burgess R, Patrick D, Turner G (2001) Fluid inclusion noble gas and halogen evidence on the origin of Cu-porphyry mineralising fluids. *Geochim Cosmochim Acta* 65:2651–2668
- Kendrick MA, Burgess R, Harrison D, Bjorlykke A (2005) Noble gas and halogen evidence for the origin of Scandinavian sandstone-hosted Pb-Zn deposits. *Geochim Cosmochim Acta* 69:109–129
- Kesle SE, Martini AM, Appold MS, Walter LM, Hston TJ, Furman FC (1996) Na-Cl-Br systematics of fluid inclusions from Mississippi Valley-type deposits, Appalachian basin: constraints on solute origin and migration paths. *Geochim Cosmochim Acta* 60:225–233
- Kracek FC (1946) Phase relations in the system silver-sulfur and the transitions in silver sulfide. *Trans Am Geophys Union* 27:367–374
- Leistel JM, Qadrouci A (1991) Le gisement argentifère d'Imiter (protérozoïque supérieur de l'Anti-Atlas, Maroc): contrôles des minéralisations, hypothèse génétique et perspectives pour l'exploration. *Chroniques Recherche Minière* 502:5–22
- Levresse G (2001) Contribution à l'établissement d'un modèle génétique des gisements d'Imiter (Ag-Hg) Bou Madine (Pb-Zn-Cu-Au) et Bou Azzer (Co-Ni-As-Au-Ag) dans l'Anti-Atlas marocain. Unpublished Ph.D. thesis, Université INPL-Nancy, 191 pp
- Levresse G, Cheilletz A, Gasquet D, Reisberg L, Deloule E, Marty B, Kyser K (2004) Osmium, sulphur, and helium isotopic results from the giant Neoproterozoic epithermal Imiter silver deposit, Morocco: evidence for a mantle source. *Chem Geol* 207:59–79
- Marcoux E, Wadjiny A (2005) Le gisement Ag-Hg de Zgounder (Jebel Siroua, Anti-Atlas, Maroc): un épithermal néoprotérozoïque de type Imiter. *Comptes Rendus Geosci* 337:1439–1446
- Marini F, Ouguir H (1990) Un nouveau jalon dans l'histoire de la tension pre-panafricaine au Maroc: le précambrien II des boutonnières du Jbel Saghro nord-oriental (Anti-Atlas, Maroc). *Comptes Rendus Acad Sci Paris* 310:577–582
- Mifdal A, Peucat JJ (1985) Datations U/Pb et Rb/Sr du volcanisme acide de l'Anti-Atlas marocain et du socle sous-jacent dans la région de Ouarzazate. Apport au problème de la limite Précambrien-Cambrien. *Sci. Géol. Bull.*, 38:185–200
- Newman HR (2009) Morocco and Western Sahara. U.S. Geological Survey 2009 Minerals Yearbook. <http://minerals.usgs.gov/minerals/pubs/country/2009/myb3-2009-mo-wi.pdf>
- Oberthür T, Melcher F, Henjes-Kunst F, Gerdes A, Stein H, Zimmerman A (2007) Hercynian age of the cobalt-nickel-arsenide-(gold) ores, Bou Azzer, Anti-Atlas, Morocco: Re-Os, Sm-Nd, and U-Pb age determinations. *Econ Geol* 104:1065–1079
- Ouguir H, Macaudière J, Dagallier G (1996) Le protérozoïque supérieur d'Imiter, Saghro oriental, Maroc: un contexte géodynamique d'arrière-arc. *J Afr Earth Sci* 22:173–189

- Ouguir H, Macaudière J, Dagallier G, Qadrouci A, Leistel JM (1994) Cadre structural du gîte Ag–Hg d’Imiter (Anti-Atlas, Maroc): implications métallogéniques. *Bull Soc Géol France* 165:233–248
- Pašava J (1994) Geochemistry and role of anoxic sediments in the origin of the Imiter silver deposit in Morocco. *Czech Geol Surv Bull* 69:1–11
- Pelleter E, Cheilletz A, Gasquet D, Mouttaqi A, Annich M, El Hakour A, Feraud G (2008) The Variscan Tamlalt-Menhouhou gold deposit, eastern High-Atlas, Morocco. *J Afr Earth Sci* 50:204–214
- Pelleter E, Cheilletz A, Gasquet D, Mottaqi A (2010) Alteration processes and impacts on regional-scale element mobility and geochronology, Tamlalt-Menhouhou deposit, Morocco. *Geol Assoc Canada, Short Course Notes* 20:177–185
- Piqué A, Bouabdelli M, Soulaïmani A, Youbi N, Iliani M (1999) Les conglomérats du P III (Néoprotérozoïque supérieur) de l’Anti Atlas (Sud du Maroc): molasses panafricaines, ou marqueurs d’un rifting fini-proterozoïque? *Comptes Rendus Acad Sci Paris* 328:409–414
- Popov AG (1995) Gisement argentifère d’Imiter: étude minéralogique, paragenèse et zonalité du gisement. Unpublished Report, Société Minière d’Imiter, Tinghir, Maroc, 115 pp
- Popov AG, Belkasmi A, Qadrouci A (1986) Le gisement argentifère d’Imiter: synthèse géologique, résultats des recherches de 1985 et bilan des réserves au 31/12/1985. Unpublished Report, Société Minière Imiter, Tinghir, Maroc, 134 pp
- Roedder E (1984) Fluid inclusions. *Rev Mineral* 12:1–644
- Simmons SF, White NC, John DA (2005) Geological characteristics of epithermal precious and base metal deposits. In: Hedenquist JW, Thompson JFH, Goldfarb RJ, Richards JP (eds) *Economic geology 100th anniversary volume, 1905–2005*, pp 485–522
- Spear N, Holland HD, Garcia-Veigas J, Lowenstein TK, Giegengack R, Peters H (2014) Analyses of fluid inclusions in Neoproterozoic marine halite provide oldest measurement of seawater chemistry. *Geology* 42:103–106
- Stacey JS, Kramers JD (1975) Approximation of terrestrial lead isotope evolution by a two-stage model. *Earth Planet Sci Lett* 26:207–221
- Thomas RJ, Fekkak A, Ennih N, Errami E, Loughlin ES, Gresse PG, Chevallier LP, Liégeois JP (2004) A new lithostratigraphic framework for the Anti-Atlas orogen, Morocco. *J Afr Earth Sci* 39:217–226
- Tritlla J, Cardellach E, Sharp ZD (2001) Origin of vein hydrothermal carbonates in Triassic limestones of the Espadán Ranges (Iberian Chain, E Spain). *Chem Geol* 172:291–305
- Tuduri J, Chauvet A, Ennaciri A, Barbanson L (2005) Model of formation of the Imiter silver deposit (eastern Anti-Atlas, Morocco): new structural and mineralogical constraints. *Comptes Rendus Géosci* 338:253–261
- Vargas JM (1983) Etude métallographique des minéralisations mercuro-argentifère d’Imiter. Rapport Fondation Scientifique Géologie Applic, Nancy 358 pp
- Villemant B, Boudon G (1999) H₂O and halogen (F, Cl, Br) behaviour during shallow magma degassing processes. *Earth Planet Sci Lett* 168:271–286
- Vlastélic G, Menard A, Gannoun JL, Piro T, Staudacher V (2013) Magma degassing during the April 2007 collapse of Piton de la Fournaise: the record of semi-volatile trace elements (Li, B, Cu, In, Sn, Cd, Re, Tl, Bi). *J Volcanol Geoth Res* 254:94–107
- Zartman RE, Doe BR (1981) Plumbotectonics—the model. *Tectonophysics* 75:135–162
- Zheng Y-F (1999) Oxygen isotope fractionation in carbonate and sulfate minerals. *Geochem J* 33:109–126

Mineral Deposits of North Africa

Bouabdellah, M.; Slack, J.F. (Eds.)

2016, XI, 594 p. 225 illus., 157 illus. in color., Hardcover

ISBN: 978-3-319-31731-1